

Spin conservation of cosmic filaments

Ming-Jie Sheng,¹ Sijia Li,¹ Hao-Ran Yu,^{1,*} Wei Wang,^{2,3} Peng Wang,⁴ and Xi Kang^{2,5}

¹*Department of Astronomy, Xiamen University, Xiamen, Fujian 361005, China*

²*Purple Mountain Observatory, Nanjing, Jiangsu 210034, China*

³*School of Astronomy and Space Science, University of Science and Technology of China, Hefei, Anhui 230026, China*

⁴*Leibniz-Institut für Astrophysik Potsdam, An der Sternwarte 16, D-14482 Potsdam, Germany*

⁵*Zhejiang University-Purple Mountain Observatory Joint Research Center for Astronomy, Zhejiang University, Hangzhou, Zhejiang 310027, China*

(Dated: April 4, 2022)

Cosmic filaments are the largest collapsing structure in the Universe. Recently both observations and simulations inferred that cosmic filaments have coherent angular momenta (spins). Here we use filament finders to identify the filamentary structures in cosmological simulations and study their physical origins, which are well described by the primordial tidal torque of their Lagrangian counterpart regions—protofilaments. This initial angular momenta statistically preserve their directions to low redshifts. We further show that a spin reconstruction method can predict the spins of filaments and potentially relate their spins to the initial conditions of the Universe. This correlation provides a new way of constraining and obtaining additional information of the initial perturbations of the Universe.

I. INTRODUCTION

The large scale structure (LSS) of the Universe contains plenty of cosmological information and enables us to answer questions about the initial state of the Universe [1]. The key procedure is looking for linear mappings from the observables at low redshifts to the properties of the initial perturbations at high redshifts [2, 3]. The nonlinear clustering of LSS leaves linear Fourier modes only $k \lesssim 0.2 h \text{ Mpc}^{-1}$, and even with reconstruction methods [4, 5] the available linear Fourier modes are still limited. It is thus valuable to find observables that relate to the initial perturbations.

Beside using the locations and velocities of galaxies to study LSS, the rotations of galaxies provide another degree of freedom to constrain the initial conditions and cosmological parameters. At low redshifts, the galaxy angular momenta (spins) are observable via their ellipticity, projection angles, spiral parities, and Doppler effects [6] and are physically related to initial perturbations. The tidal torque theory explains how the angular momentum of a clustering system is generated in Lagrangian space [1, 7, 8], where the mass elements are described in their initial comoving coordinates. It is also confirmed by many cosmological simulations that the tidal torque of protohalos (dark matter halos in Lagrangian space) generated by the misalignment between the moment of inertia and the tidal field provides a persistent generation of angular momentum until virialization of halos [9, 10]. Also, hydrodynamical simulations show that the spins of galaxies tend to align with their host halos [11]. These facts make galaxy spins another observable in constraining initial perturbations [12, 13]. Reference [14] found a method to reconstruct galaxy spins by initial perturbations, and the initial conditions can be estimated by density reconstructions [15]. Reference [16] applied this method and for the first time confirmed the correlation between galaxy spins and cosmic initial conditions.

Filaments are one of the largest structures of the cosmic web [17, 18]. By numerical simulations, they have been demonstrated to be spinning in the LSS environment [19–21]. Observationally,

[22] for the first time detected possible evidence for filament spins by examining the velocities of galaxies perpendicular to the filament’s axis. These studies suggest that we could use the filament spins to understand the structure formation and potentially constrain cosmological models and parameters using the framework similar to galaxies. In Lagrangian space, the protofilaments could also be defined according to the mass elements of filaments in their Lagrangian space. Because filaments are generally much more massive than galaxies and halos, they occupy larger regions in Lagrangian space, corresponding to larger, more linear scales. If there is a strong correlation between Eulerian and Lagrangian filaments, they can be used to probe larger scales of the primordial perturbations complimentary to that of galaxies and halos. It is thus interesting to examine the Lagrangian properties of filaments, whether their initial spins can be described by the tidal torque theory, and whether their spins are conserved across the cosmic evolution and then can be reconstructed by the initial conditions. In this paper, we use cosmological simulations to explore the Lagrangian properties of cosmic filaments and their spin conservations.

The structure of the paper is as follows. In Sec.II, we describe the simulation configurations and filament finder for filament identifications. In Sec.III, we present the results for the spin properties, conservations, and reconstructions. In Sec.IV, we give conclusions and make discussions and prospects.

II. SIMULATION AND FILAMENT IDENTIFICATION

We use numerical simulations to study the properties of filaments, which based on the cosmological N -body simulation code CUBE [23]. We assume a flat Λ CDM cosmology with cosmological parameters $\Omega_m = 0.3$, $\Omega_\Lambda = 0.7$, $\sigma_8 = 0.87$, $h = 0.7$, in a cubic box $L = 100 \text{ Mpc}/h$ per side with periodic boundary conditions. $N_p = 512^3$ particles are initially uniformly initialized in Lagrangian space, and the “grid initial condition” is used where Lagrangian positions of particles are placed at the each center of the cell, in a $N_g = 512^3$ mesh, so it is straightforward to acquire their Lagrangian properties. The particles are then assigned with initial linear displacements and initial velocities by using

* haoran@xmu.edu.cn

the Zel'dovich approximation [24] at initial redshift $z_{\text{init}} = 100$, and then are evolved to Eulerian space at redshift $z = 0$ using the particle-particle particle-mesh force calculation. The particle mass is approximately $8.8 \times 10^8 M_\odot$.

Since filaments not self-bound by gravity and density dependency alone, there is no standard definition of cosmic filaments, resulting in many different filament finder realizations. According to their discrepancies of definitions, they can be classified by more mathematical and more physical ways. Mathematically, skeleton (e.g., the discrete persistent structure extractor [25–27]), graph theory (e.g., state-of-the-art tracer T-Rex [28], MST [29]), and Bayesian [30–32] methods extract the filament spine. Reference [33] developed a novel method to find filaments in terms of machine learning. Many theories (pancake model, hierarchical clustering) interpret LSS formation subjected to the tidal field tensor, defined by the Hessian matrix of the overdensity field, $H_{ij} = \partial_i \partial_j \delta$, where $\delta \equiv \rho/\langle\rho\rangle - 1$ is the overdensity. Accordingly many physical methods to trace cosmic web, including filaments, are based on Hessian matrix by single scale [34–36] or multiscales [37–39].

In this paper, we adopt the Smoothed Hessian Major Axis Filament Finder (SHMAFF) [35], which, physically, starts from the tensor field H_{ij} to define the filament spine. Here we briefly introduce the primary parameters for completeness, and more details can be found in [35]. For adapting the spine to the density field, we allocate all dark matter particles to a mesh with grid number $N_g = 256^3$ by cloud-in-cell mass assignment, and smooth it with a $R_s = 2 \text{ Mpc}/h$ Gaussian kernel. For each grid, we eigendecompose the matrix H_{ij} into eigenvalues $\lambda_1 < \lambda_2 < \lambda_3$ and eigenvectors \mathbf{A}_i ($i = 1, 2, 3$). Intuitively, filament skeletons satisfy $\delta > 0$ and $\lambda_2 < 0$, whereas \mathbf{A}_3 represents the alignment of the skeleton.¹ We first remove all the grids satisfying any of the following criteria:

$$\delta < 0, \lambda_2 \geq 0. \quad (1)$$

Then, we start from the grid at the minimum λ_1 and iteratively search for the adjacent grids along both directions, $\pm \mathbf{A}_3$, until the grid either satisfies the removal criteria (1), or the $|\mathbf{A}_3|$ angle between two grid candidates exceeds a given threshold C , i.e.,

$$|\mathbf{A}_{3,n} \times \mathbf{A}_{3,n-1}| > \sin(C\Delta), \quad (2)$$

where Δ is the cell width. We take the angle value of $C = 30^\circ R_s^{-1}$. Note that we remove the grids of cylinder within width W_i at each step as

$$W_i = K \sqrt{\frac{-\rho_i}{\lambda_{1,i}}}, \quad (3)$$

where K is set to 2 in this work. The filament particles are identified by the criterion that their vertical distance to the skeleton are less than $2 \text{ Mpc}/h$.

By applying the filament finder we get a filament catalog with 1680 filaments. This catalog contains the detailed information about the filament skeletons and particles. In the left panel of Fig. 1, we plot the skeletons of all filaments in the simulation box.

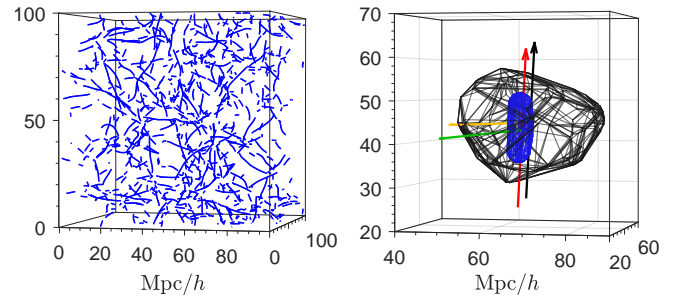


FIG. 1. Visualization of filaments. The left panel shows the skeletons of identified filaments in the simulation volume. The right panel shows the convex hull of a filament in Lagrangian (gray) and Eulerian (blue) spaces. The mass of the selected filament is $1.05 \times 10^{15} M_\odot$. The black and red arrows represent the direction of spines of the filament in Lagrangian and Eulerian spaces and the yellow and green arrows represent the directions of their angular momenta, respectively.

III. RESULTS

A. Mass distributions

In this section we start with a comparison between filament properties in Eulerian and Lagrangian spaces. The protofilaments are obtained by using particle IDs in the N -body simulation and tracing back to their Lagrangian positions. We use moment of inertia tensor $I_{ij} = \sum_i m_i x'_i x'_j$ to characterize the mass distribution of a system up to quadrupole. Here m_i is the particle mass, and \mathbf{x}' is the particle position relative to the center of mass in Eulerian or Lagrangian space in consideration. The eigendecomposition of I_{ij} gives the the primary, intermediate, and minor axes of the mass distribution of the filament and their alignments in space. The eigenvalues are sorted as $i_1 > i_2 > i_3$, so the the primary axis i_1 , associated with the eigenvector \mathbf{V}_1 (hereafter we denote \mathbf{V}_j as the eigenvector of i_j , $j = 1, 2, 3$) is expected to align with the spine of the filament. The properties of the mass distribution can be characterized by three parameters, the trace $\tau = i_1 + i_2 + i_3$, the ellipticity $e = (i_1 - i_3)/2\tau$, and the prolateness $p = (i_1 - 2i_2 + i_3)/2\tau$ [40]. A perfect sphere has $e = p = 0$, a thin disk has $e = 1/4$ and $p = -1/4$, while a slim straight filament has $e = 1/2$ and $p = 1/2$.

In the top panels of Fig. 2, we plot the joint probability distribution functions (PDFs) of ellipticity e and prolateness p for all 1680 filaments in Lagrangian and Eulerian spaces, respectively, and the one-dimensional PDF marginalized along each axis. As expected, in Eulerian space, nearly all filaments show prolate ($p > 0$) mass distributions rather than oblate ($p < 0$). In terms of the expectation value of the distribution, $\langle p_{\text{Eul}} \rangle = 0.25$. Meanwhile, the filaments show systematic ellipticity, $\langle e_{\text{Eul}} \rangle = 0.33$. In the bottom panels of Fig. 2, we plot the dependence of e and p of filaments in Eulerian space with spine length and mass respectively, where spine length is represented by $\sqrt{i_1}$. Filaments with longer spine length tend to have $(e, p) \rightarrow (1/2, 1/2)$, but this trend shows weak dependence on mass. Note that there are still few filaments with low or negative prolateness, and with low ellipticity. These filaments are generally shorter and less massive and the inclusion of particles involve numerical artifacts. However in later

¹ We note that H_{ij} is parity even, so in the eigendecompositions, \mathbf{A}_i is “arrowless.”

subsections they do not affect the conclusions. In contrast, the protofilaments in Lagrangian space tend to be more spherical relatively. In the top left panel of Fig.2, the joint PDF does not cluster to the $(e, p) = (1/2, 1/2)$ corner. Numerically the statistics of these two parameters in Lagrangian space are $\langle p_{\text{Lag}} \rangle = 0.12$ and $\langle e_{\text{Lag}} \rangle = 0.26$.

These results illustrate the filament formation picture in the structure evolution. The protofilament region is more spherical rather than filamentary initially. While in contrast to protohalos, which collapse in all directions, protofilaments primarily collapse along two directions, \mathbf{V}_2 and \mathbf{V}_3 , due to the external tidal field. Because the initial spin given by the tidal torque is preferentially aligned with \mathbf{V}_2 and the second principal axis of the tidal tensor \mathbf{T}_2 [13] (hereafter we denote \mathbf{T}_i and t_i as the eigenvectors and eigenvalues of \mathbf{T}), we thus expect that in the anisotropic collapse of filaments, the tidal torque is also preferentially aligned with \mathbf{V}_2 . In the following section we indeed find that both Lagrangian and Eulerian filament spins are preferentially aligned with \mathbf{V}_2 ; i.e., the spin vectors are preferentially perpendicular to the spine of the filaments \mathbf{V}_1 . Besides, a spherical Lagrangian region is potentially suitable to directly apply the spin reconstruction methods presented in [14].

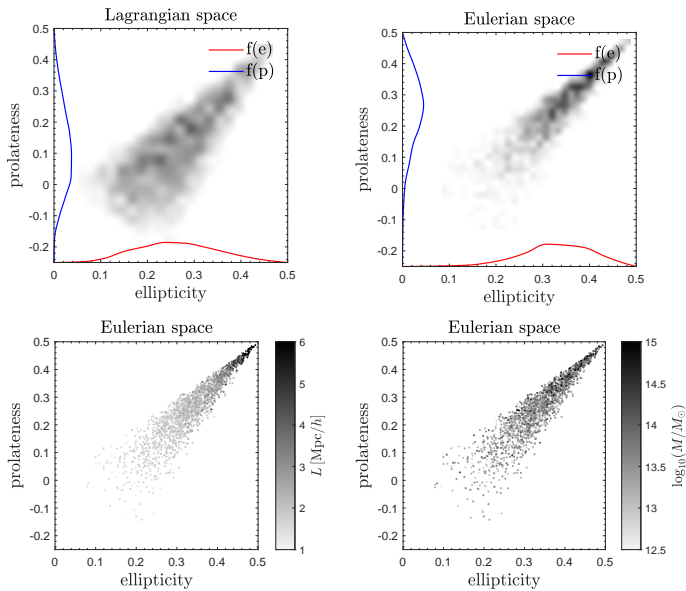


FIG. 2. Joint PDFs of ellipticity e and prolateness p for filaments in Lagrangian (top left panel) and Eulerian (top right panel) spaces, shown by gray scale. The red and blue curves represent the PDFs of e and p , respectively. The bottom panels are the same as the top right panel, but points are colored according to the spine length of the filaments (bottom left panel) and the mass of the filaments (bottom right panel).

B. Spin directions and conservations

Here we study the angular momentum properties of filaments. We use \mathbf{j} to denote the angular momentum vector. In Eulerian space, the angular momentum vector of a filament is defined as $\mathbf{j}_E = \sum_i m_i (\mathbf{x}_i - \bar{\mathbf{x}}) \times \mathbf{v}_i = \sum_i m_i \mathbf{x}'_i \times \mathbf{v}_i$, where m_i , \mathbf{x}_i , $\bar{\mathbf{x}}$ and \mathbf{v}_i

are the particle mass, Eulerian position, Eulerian center of mass, and Eulerian velocity, respectively. $\mathbf{x}'_i \equiv \mathbf{x}_i - \bar{\mathbf{x}}$ is the position relative to the center of mass $\bar{\mathbf{x}}$. In Lagrangian space, the angular momentum vector is similarly defined as $\mathbf{j}_L = \sum_i m_i \mathbf{q}'_i \times \mathbf{u}_i = \sum_i m_i (\mathbf{q}_i - \bar{\mathbf{q}}) \times \mathbf{u}_i = \sum_i m_i \mathbf{q}'_i \times (-\nabla \phi|_{\mathbf{q}_i})$, where \mathbf{q}_i , $\bar{\mathbf{q}}$, \mathbf{u}_i are the Lagrangian position, Lagrangian center of mass, Lagrangian velocity, respectively. $\mathbf{q}'_i \equiv \mathbf{q}_i - \bar{\mathbf{q}}$ is the Lagrangian position relative to Lagrangian center of mass $\bar{\mathbf{q}}$. The Lagrangian velocity \mathbf{u}_i is simply expressed by the gradient of the primordial gravitational potential ϕ , consistent with our setup in the initial conditions [24].

We use the cosine of the angle between two vectors \mathbf{j}_L and \mathbf{j}_E to quantify the cross-correlation between their directions, i.e., $\mu(\mathbf{j}_L, \mathbf{j}_E) \equiv \mathbf{j}_L \cdot \mathbf{j}_E / (|\mathbf{j}_L| |\mathbf{j}_E|) \in [-1, 1]$. The μ of two randomly distributed vectors in three-dimensional space is top-hat distributed between -1 and 1 , with expectation 0 . In Fig.3, we plot the PDF of $\mu(\mathbf{j}_L, \mathbf{j}_E)$ for all filaments. The expectation value $\langle \mu \rangle$ takes 0.70 and the PDF of $\mu(\mathbf{j}_L, \mathbf{j}_E)$ obviously depart from a top-hat distribution, suggesting that $\mathbf{j}_L, \mathbf{j}_E$ directions are strongly correlated. This property is similar to the spin conservations of dark matter halos [41]. Next we decompose the spin vector into parallel and perpendicular components with respect to the major axis \mathbf{V}_1 (spine) of the Eulerian filament. From now on, we denote them with superscripts \parallel and \perp . In the first two insets of Fig.3, we plot the PDFs of $|\mathbf{j}_L^\parallel|/|\mathbf{j}_L| = |\mu(\mathbf{j}_L, \mathbf{V}_1)|$ and $|\mathbf{j}_E^\parallel|/|\mathbf{j}_E| = |\mu(\mathbf{j}_E, \mathbf{V}_1)|$, which show that in both Lagrangian and Eulerian spaces, the spin directions are preferably perpendicular to the spine of the Eulerian filaments. This is consistently explained by the tidal torque theory, which expresses the initial tidal torque spin as $j_i \propto \epsilon_{ijk} I_{jl} T_{lk}$, where ϵ_{ijk} is the Levi-Civita symbol and $T_{lk} \propto -\partial_l \partial_k \phi$ is the tidal tensor. In the coordinate system of principal axes of \mathbf{T} , $j_2 \propto (t_1 - t_3) I_{31}$ is the dominated component due to the largeness of $t_1 - t_3$ [for more details, see Eq.(2) and the following discussions of [13]]. In comparison, the filament spine \mathbf{V}_1 is aligned with the least collapsing direction \mathbf{T}_1 , and $\mathbf{T}_1 \perp \mathbf{T}_2$. The third inset of Fig.3 confirms it numerically by the PDF of $\mu(\mathbf{T}_2, \mathbf{V}_1)$ and thus explains the dominated spin component $j_2 \perp \mathbf{V}_1$ statistically.

To understand the spin directions more intuitively, we select a typical filament with mass $1.05 \times 10^{15} M_\odot$ in our simulation and visualize its shapes in Lagrangian and Eulerian spaces, as well as the spin vectors in both spaces in the right panel of Fig.1. The shape is visualized by the convex hull of all particles belonging to the filament, either in Eulerian (blue) or Lagrangian (gray) space. Consistent with the statistics of Fig.2, the Eulerian filament is elongated vertically, whereas its Lagrangian counterpart is more spherical. The yellow and green arrows show their spins, and the black and red arrows represent their components in the major axis \mathbf{V}_1 . Their magnitudes are normalized arbitrarily for better visualization. The conservation of spin directions is seen by this typical filament.

C. Spin magnitudes

In this subsection we focus on the conservation of spin magnitudes. The comparison of angular momentum magnitudes through the cosmic evolution is conveniently analyzed by the dimensionless spin parameter. The spin magnitude of a system in Eulerian space can be characterized by a dimensionless kinematic

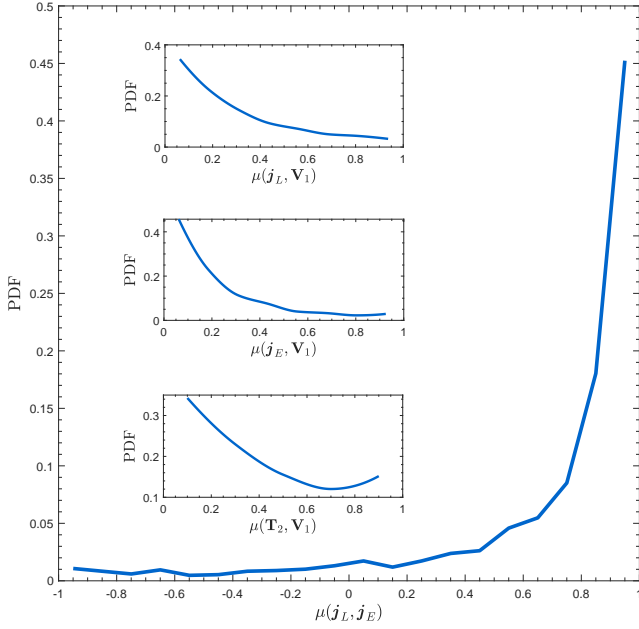


FIG. 3. Spin conservation of cosmic filaments shown by PDF of $\mu(j_L, j_E)$. The distribution shows a strong deviation from a top-hat distribution, suggesting that the filament spin directions are conserved from high redshifts to low redshifts. The three insets are the PDFs of $\mu(j_L, \mathbf{V}_1)$, $\mu(j_E, \mathbf{V}_1)$ and $\mu(\mathbf{T}_2, \mathbf{V}_1)$, where \mathbf{T}_2 denotes the second principal axis of the tidal tensor.

spin parameter λ_{KE} [41], which is defined as

$$\lambda_{KE} \equiv \frac{\int_{V_x} \hat{j}_i \epsilon_{ijk} x'_j v'_k dM}{\int_{V_x} x' v' dM} = \frac{\int_{V_x} \sin \theta_1 \cos \theta_2 x' v' dM}{\int_{V_x} x' v' dM}, \quad (4)$$

where $\hat{j} = (\mathbf{j}_E / j_E)$ is the unit \mathbf{j}_E vector ($j_E = |\mathbf{j}_E|$), $x' = |\mathbf{x}'|$, $v' = |\mathbf{v}'| \equiv |\mathbf{v} - \bar{\mathbf{v}}|$ is the velocity relative to the average velocity of the filament $\bar{\mathbf{v}}$, $\sin \theta_1 = \sqrt{1 - \mu^2(\mathbf{x}', \mathbf{v}')}$ and $\cos \theta_2 = \mu(\mathbf{x}' \times \mathbf{v}', \mathbf{j}_E)$, which can be similarly defined in Lagrangian space and denoted with λ_{KL} . They take the value $[0, 1]$ and describe whether a system is more velocity dispersion supported or rotation supported. For dark matter halos and their protohalos in Lagrangian space, [41] demonstrated that both spin directions and spin magnitudes tend to be correlated across cosmic evolution.

For two variables X, Y , the correlation coefficient is defined as

$$r(X, Y) = \frac{\text{Cov}(X, Y)}{\sqrt{\text{Var}[X] \cdot \text{Var}[Y]}}, \quad (5)$$

and the covariance is normalized by the square root of the multiplication of their autovariances. The correlation $r \in [-1, 1]$, statistically $r = \pm 1$, indicates the strongest correlation/anticorrelation, and $r \approx 0$ indicates a noncorrelation.

In Fig.4, we plot the correlation between λ_{KL} and λ_{KE} for filaments in different length ranges. Table I lists the number of filament samples and the correlation coefficient $r(\lambda_{KL}, \lambda_{KL})$ as a function of filament spine length range. Figure 4 and Table I suggest that the spin magnitudes of \mathbf{j}_L and \mathbf{j}_E have a strong positive correlation. We find that this positive correlation is related to the length of the spine. Filaments with longer spines tend to have

a stronger correlation between λ_{KL} and λ_{KE} . This trend can be explained by the fact that longer filaments tend to be more filamentary in our samples as we have shown in the bottom left panel of Fig.2, which is partly a consequence of the limitation of the filament finder. By eliminating those filaments with low prolateness and ellipticity could make the correlation more robust.

By observing the PDFs of single parameters, we find that the values of λ_L and λ_E are much less than unity, suggesting that the filaments are not rotation supported in both Eulerian and Lagrangian spaces. This behavior is very similar to dark matter halos and protohalos by various of definitions [41].

To compare with the current observation works [22], which detected observational evidence for \mathbf{j}^\parallel , it is interesting to extract the spin magnitudes of \mathbf{j}^\parallel , which is parallel to the spine (\mathbf{V}_1), and check whether it is correlated to their spin magnitudes in Lagrangian space. By projecting Eq.(4) onto a plane perpendicular to \mathbf{V}_1 , the kinematic spin parameter becomes

$$\lambda_E^\parallel \equiv \frac{\hat{\mathbf{V}}_1 \cdot \mathbf{j}_E^\parallel}{\sum x'^\perp v'^\perp}, \quad (6)$$

where $x'^\perp = |\mathbf{x}'^\perp|$, $v'^\perp = |\mathbf{v}'^\perp|$, vectors with \perp are the components perpendicular to the spine. Here $\hat{\mathbf{V}}_1$ is an unit vector aligned with the spine. Because the spine is parity even, the sign of λ_E^\parallel is defined according to the arbitrarily chosen $\hat{\mathbf{V}}_1$. Similarly, λ_L^\parallel can be obtained from \mathbf{j}_L^\parallel in the same manner,

$$\lambda_L^\parallel \equiv \frac{\hat{\mathbf{V}}_1 \cdot \mathbf{j}_L^\parallel}{\sum q'^\perp u'^\perp}. \quad (7)$$

With the above definition, $|\lambda_L^\parallel|, |\lambda_E^\parallel| \in [0, 1]$, and larger $|\lambda_L^\parallel|$ or $|\lambda_E^\parallel|$ corresponds to more coherent rotations along the spine. Meanwhile, same/different signs of λ_L^\parallel and λ_E^\parallel indicates that \mathbf{j}_E^\parallel is parallel/antiparallel to \mathbf{j}_L^\parallel .

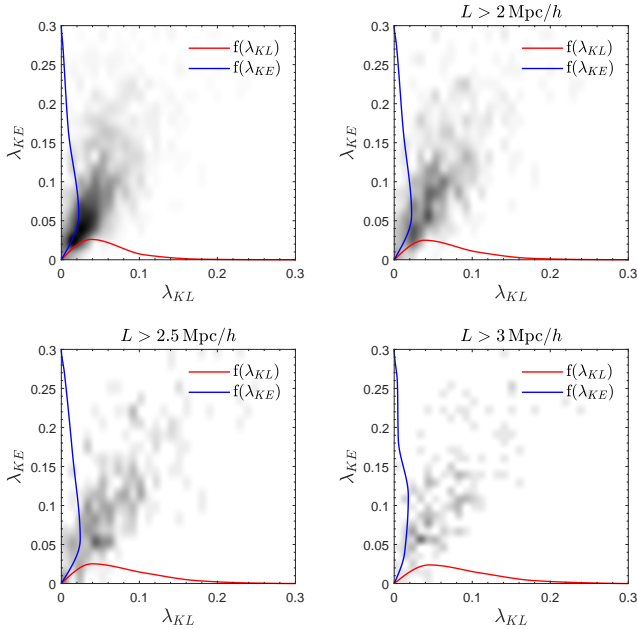
In Fig.5, we plot the correlation between λ_L^\parallel and λ_E^\parallel for filaments in different length ranges. The correlation coefficients $r(\lambda_L^\parallel, \lambda_E^\parallel)$ in different spine length range are also listed in Table I. We find that the parallel component of the spin shows similar correlation as \mathbf{j} , the spin magnitudes of \mathbf{j}_L^\parallel and \mathbf{j}_E^\parallel have a strong positive correlation and filaments with longer spines tend to have a stronger correlation. Besides, the absolute values of λ_L^\parallel and λ_E^\parallel are also much less than unity, but fortunately the smallness of the rotation component of the filaments can still be measured [22].

D. Spin reconstruction

In this subsection we reconstruct the predicted spins for filaments based on their Lagrangian space properties analogous to the spin reconstruction of halos. As we have mentioned in Sec.III, the initial angular momentum vector of a protohalo that initially occupies Lagrangian volume V_L is approximately by $\mathbf{j} \propto \epsilon_{ijk} \mathbf{I}_{jl} T_{lk}$, where $\mathbf{I} = (I_{jl})$ is the moment of inertia tensor of V_L , $\mathbf{T} = (T_{lk})$ is the tidal tensor acting on \mathbf{I} , and ϵ_{ijk} is the Levi-Civita symbol collecting the antisymmetric components generated by the misalignment between \mathbf{I} and \mathbf{T} . The spin reconstruction of dark matter

TABLE I. Number of filament samples and the correlation coefficient as a function of filament spine length range.

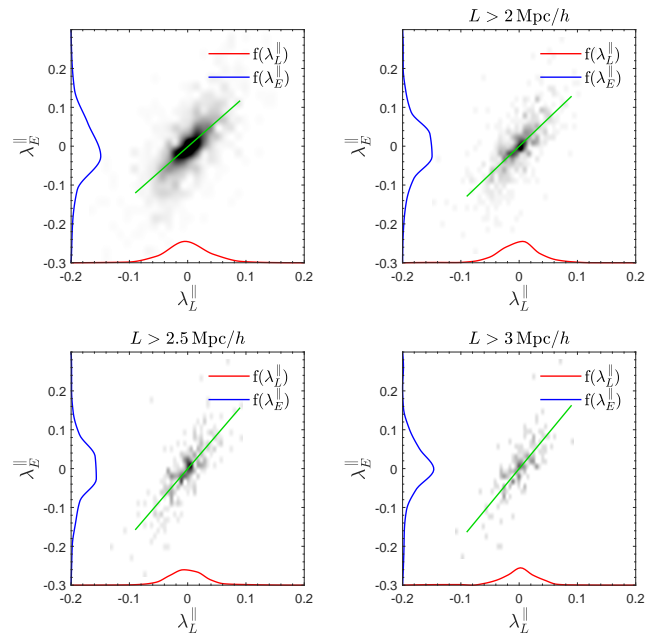
Spine length	$L > 0 \text{ Mpc}/h$	$L > 2 \text{ Mpc}/h$	$L > 2.5 \text{ Mpc}/h$	$L > 3 \text{ Mpc}/h$
Sample number	1680	746	326	177
$r(\lambda_{KL}, \lambda_{KE})$	0.57	0.61	0.712	0.717
$r(\lambda_L^{\parallel}, \lambda_E^{\parallel})$	0.67	0.70	0.771	0.774

FIG. 4. Correlation between λ_{KL} and λ_{KE} for filaments in different length ranges. The gray scale in the background represents their joint distribution and the red and blue curves represent the PDFs of the parameters indicated by the label of each axis.

halos is by defining [14]

$$\mathbf{j}_R = (j_i) \propto \epsilon_{ijk} \mathcal{T}_{jl} \mathcal{T}_{lk}^+, \quad (8)$$

where $\mathcal{T}, \mathcal{T}^+$ are tidal fields constructed as Hessians of the initial gravitational potential smoothed at two different scales r, R . The initial gravitational potential can be estimated by the initial density field reconstructed method ELUCID, for which we refer the readers to [15, 42] for more details. This method can reproduce the density field of the nearby universe generated from the galaxy distributions in observation. To obtain \mathcal{T} and \mathcal{T}^+ , we smooth the initial gravitational potential $\phi_{\text{init}}(\mathbf{q})$, by multiplying it in the Fourier space by the baryonic acoustic oscillation damping model $\mathcal{D}(k)^{1/4} = \exp(-r^2 k^2/2)^{1/4}$ [4]. By choosing $R \rightarrow r_+$, we find \mathbf{j}_R a good approximation for an angular momentum of a protohalo. Similarly, we apply this method to protofilaments, then we get the spin field \mathbf{j}_R reconstructed from known initial conditions. We group all identified filaments into five mass bins, ranging from $\sim 10^{12} M_\odot$ to $\sim 10^{15.5} M_\odot$, then apply Eq.(8) with a set of different smoothing scales r , and compute the correlations between

FIG. 5. The same as Fig.4 but for λ_L^{\parallel} and λ_E^{\parallel} . The green lines are the linear fittings of all data points.

reconstructed and Eulerian spins of filaments. In Fig.6, we plot $\mu(\mathbf{j}_E, \mathbf{j}_R)$ as a function of smoothing scales r and filament mass bins. The gray scale shows the degree of correlation and the darkest region in each mass bin represents the optimal smoothing scale r_{opt} , also indicated by the yellow dashed curve.

We find that the spins of more massive filaments can generally be predicted at a wide range of smoothing scales. The correlation is larger than 0.3 for filaments more massive than $10^{13.5} M_\odot$. We also find that more massive filaments are better reconstructed by a larger smoothing radius, and this behavior is similar to the spin reconstruction of dark matter halos [14]. As a reference, we plot with the red dashed curve the equivalent protofilament radius in the Lagrangian space defined as $r_q \equiv (2MG/\Omega_m H_0^2)^{1/3}$. We find that r_{opt} is not closely related to r_q , and find $\sim 5 \text{ Mpc}/h$ a universal smoothing scale for all massive filaments.

IV. CONCLUSION AND DISCUSSIONS

In this paper, by using numerical simulations, we study the angular momentum properties of cosmic filaments across the cosmic

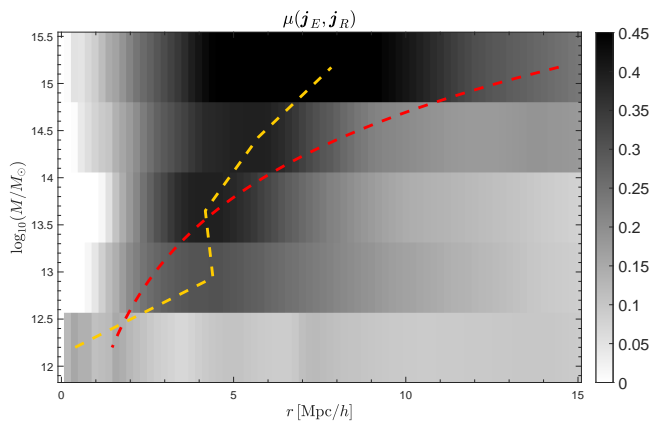


FIG. 6. Correlation between the Eulerian \mathbf{j}_E filament spins and spins reconstructed using Eq.(8) from known initial conditions \mathbf{j}_R . The gray scale in the background shows the degree of correlation and darker colors show better reconstruction. The red and yellow dashed represent the Lagrangian equivalent protofilament radius r_q and optimal smoothing scale r_{opt} , respectively.

evolution, as well as their origins, conservations, and predictability. The conclusion of our results is summarized as follows:

- In terms of moment of inertia tensors and their eigendecompositions, the cosmic filaments in Lagrangian space (protofilaments) exhibit much more spherical shapes, for which Lagrangian spin reconstruction method with an isotropic smoothing function is effective to be applied for the angular momentum prediction.
- The angular momentum directions of filaments and their protofilaments are very well correlated, with a statistical correlation of 0.7, and significantly depart from a random distribution from uncorrelated pairs of vectors. This shows that the angular momentum directions of filaments are well conserved through the cosmic evolution, similar to that of dark matter halos.
- The angular momentum direction is more perpendicular to the spine (major axis) of the filament, which can be well predicted by tidal torque theory, whereas the spin component parallel to the spine matches the numerical and observational analysis of filaments in previous studies.
- By constructing a dimensionless spin parameter of this spin and its parallel component, we find that the kinematic mo-

tion of the filaments relatively less rotation supported. This statistics is very similar to that of dark matter halos.

- The dimensionless spin magnitudes of protofilaments and filaments are statistically significantly correlated, showing that faster spinning protofilaments are more likely to form faster spinning filaments at low redshifts.
- The filament spins can be predicted by a spin reconstruction method in Lagrangian space, and the predictability is similar to the spin reconstruction of dark matter halos. This opens up the possibility of using filament spins to constrain the cosmic initial conditions.

We notice that the above conclusions weakly depend on the mass and length of the filaments, with longer and more massive filaments having better spin conservation and predictability. This can be partly explained by the limitation of filament finders, meaning that those short and low massive samples in the catalog might be fake filament structures and that eliminating them could make the results more robust. The free parameters in our filament finder and other available filament finder algorithms add freedom in the identifications of filaments and their containing particles. As a convergence test, we also use different parameters in our filament finder discussed in Sec.II and they all give consistent results. Discovering other filament finder methods and comparing the results are not included in this paper and can be left to future studies.

However, it is more important to study how the filament spins can be observed by multiple tracers, such as galaxies and their relative velocities, e.g., [22], or intergalactic media by kinetic Sunyaev Zel'dovich effect [43]. Galaxy formation simulations in a cosmological volume are needed to understand these effects and are helpful to construct the pipeline of the analysis. Moreover, besides [21, 22], it is also valuable to extract the angular momenta perpendicular to the spines of the filaments. Multitracer reconstruction of the initial density field and redshift space distortion should be included in the analysis. We leave them to future works.

ACKNOWLEDGMENTS

We thank the anonymous referee for valuable suggestions. This work is supported by National Science Foundation of China Grants No. 11903021 and No. 12173030. P.W. and X.K. acknowledge support from the joint Sino-German DFG research Project DFG-LI 2015/5-1, NSFC No. 11861131006. The simulations were performed on the workstation of cosmological sciences, Department of Astronomy, Xiamen University.

[1] P. J. E. Peebles, *ApJ***155**, 393 (1969).
[2] C. D. Rimes and A. J. S. Hamilton, *MNRAS***360**, L82 (2005), astro-ph/0502081.
[3] M. McQuinn, *J. Cosmology Astropart. Phys.***2021**, 024 (2021), 2008.12312.
[4] H.-R. Yu, U.-L. Pen, and H.-M. Zhu, *Phys. Rev. D***95**, 043501 (2017), 1610.07112.

[5] Q. Pan, U.-L. Pen, D. Inman, and H.-R. Yu, *MNRAS***469**, 1968 (2017), 1611.10013.
[6] M. Iye, K.-i. Tadaki, and H. Fukumoto, *ApJ***886**, 133 (2019), 1910.10926.
[7] A. G. Doroshkevich, *Astrofizika* **6**, 581 (1970).
[8] S. D. M. White, *ApJ***286**, 38 (1984).
[9] C. Porciani, A. Dekel, and Y. Hoffman, *MNRAS***332**, 325 (2002), astro-ph/0105123.

- [10] H.-R. Yu, U.-L. Pen, and X. Wang, *Phys. Rev. D***99**, 123532 (2019), 1810.11784.
- [11] A. F. Teklu et al., *ApJ***812**, 29 (2015), 1503.03501.
- [12] J. Lee and U.-L. Pen, *ApJ***532**, L5 (2000), astro-ph/9911328.
- [13] J. Lee and U.-L. Pen, *ApJ***555**, 106 (2001), astro-ph/0008135.
- [14] H.-R. Yu et al., *Phys. Rev. Lett.***124**, 101302 (2020), 1904.01029.
- [15] H. Wang, H. J. Mo, X. Yang, Y. P. Jing, and W. P. Lin, *ApJ***794**, 94 (2014), 1407.3451.
- [16] P. Motloch, H.-R. Yu, U.-L. Pen, and Y. Xie, *Nature Astronomy* **5**, 283 (2021), 2003.04800.
- [17] I. B. Zeldovich, J. Einasto, and S. F. Shandarin, *Nature***300**, 407 (1982).
- [18] J. R. Bond, L. Kofman, and D. Pogosyan, *Nature***380**, 603 (1996), astro-ph/9512141.
- [19] M. C. Neyrinck, *MNRAS***460**, 816 (2016), 1510.03431.
- [20] M. Neyrinck, M. A. Aragon-Calvo, B. Falck, A. S. Szalay, and J. Wang, *The Open Journal of Astrophysics* **3**, 3 (2020), 1904.03201.
- [21] Q. Xia, M. C. Neyrinck, Y.-C. Cai, and M. A. Aragón-Calvo, *MNRAS***506**, 1059 (2021), 2006.02418.
- [22] P. Wang, N. I. Libeskind, E. Tempel, X. Kang, and Q. Guo, *Nature Astronomy* (2021), 2106.05989.
- [23] H.-R. Yu, U.-L. Pen, and X. Wang, *ApJS***237**, 24 (2018), 1712.06121.
- [24] Y. B. Zel'dovich, *A&A***5**, 84 (1970).
- [25] T. Sousbie, *MNRAS***414**, 350 (2011), 1009.4015.
- [26] T. Sousbie, C. Pichon, and H. Kawahara, *MNRAS***414**, 384 (2011), 1009.4014.
- [27] D. Novikov, S. Colombi, and O. Doré, *MNRAS***366**, 1201 (2006), astro-ph/0307003.
- [28] T. Bonnaire, N. Aghanim, A. Decelle, and M. Douspis, *A&A***637**, A18 (2020), 1912.00732.
- [29] L. A. Pereyra, M. A. Sgró, M. E. Merchán, F. A. Stasyszyn, and D. J. Paz, *MNRAS***499**, 4876 (2020), 1911.06768.
- [30] E. Tempel et al., *MNRAS***438**, 3465 (2014), 1308.2533.
- [31] R. S. Stoica, V. J. Martínez, and E. Saar, *Journal of the Royal Statistical Society: Series C (Applied Statistics)* **56**, 459 (2007).
- [32] R. S. Stoica, V. J. Martínez, and E. Saar, *A&A***510**, A38 (2010), 0912.2021.
- [33] J. Hui, M. Aragon, X. Cui, and J. M. Flegel, *MNRAS***475**, 4494 (2018), 1803.11156.
- [34] O. Hahn, C. Porciani, C. M. Carollo, and A. Dekel, *MNRAS***375**, 489 (2007), astro-ph/0610280.
- [35] N. A. Bond, M. A. Strauss, and R. Cen, *MNRAS***409**, 156 (2010), 1003.3237.
- [36] J. E. Forero-Romero, Y. Hoffman, S. Gottlöber, A. Klypin, and G. Yepes, *MNRAS***396**, 1815 (2009), 0809.4135.
- [37] M. A. Aragón-Calvo, B. J. T. Jones, R. van de Weygaert, and J. M. van der Hulst, *A&A***474**, 315 (2007), 0705.2072.
- [38] M. Cautun, R. van de Weygaert, and B. J. T. Jones, *MNRAS***429**, 1286 (2013), 1209.2043.
- [39] M. Cautun, R. van de Weygaert, B. J. T. Jones, and C. S. Frenk, *MNRAS***441**, 2923 (2014), 1401.7866.
- [40] C. Porciani, A. Dekel, and Y. Hoffman, *MNRAS***332**, 339 (2002), astro-ph/0105165.
- [41] Q. Wu, H.-R. Yu, S. Liao, and M. Du, *Phys. Rev. D***103**, 063522 (2021), 2011.03893.
- [42] H. Wang et al., *ApJ***831**, 164 (2016), 1608.01763.
- [43] E. J. Baxter, B. D. Sherwin, and S. Raghunathan, *J. Cosmology Astropart. Phys.***2019**, 001 (2019), 1904.04199.